

Tailoring interference and nonlinear manipulation of femtosecond x-rays

Marc Herzog¹, Daniel Schick¹, Wolfram Leitenberger¹,
Roman Shayduk², Renske M van der Veen^{3,4},
Christopher J Milne^{3,4}, Steven L Johnson³, Ionela Vrejoiu⁵
and Matias Bargheer^{1,2,6}

¹ Institut für Physik und Astronomie, Universität Potsdam, Karl-Liebknecht-Str. 24-25, 14476 Potsdam, Germany

² Helmholtz-Zentrum Berlin für Materialien und Energie GmbH, Hahn-Meitner-Platz 1, 14109 Berlin, Germany

³ Swiss Light Source, Paul Scherrer Institut, 5232 Villigen PSI, Switzerland

⁴ Laboratoire de Spectroscopie Ultrarapide, Ecole Polytechnique Fédérale de Lausanne, 1015 Lausanne, Switzerland

⁵ Max-Planck-Institut für Mikrostrukturphysik, Weinberg 2, 06120 Halle, Germany

E-mail: bargheer@uni-potsdam.de

New Journal of Physics **14** (2012) 013004 (9pp)

Received 14 August 2011

Published 6 January 2012

Online at <http://www.njp.org/>

doi:10.1088/1367-2630/14/1/013004

Abstract. We present ultrafast x-ray diffraction (UXRD) experiments on different photoexcited oxide superlattices. All data are successfully simulated by dynamical x-ray diffraction calculations based on a microscopic model, that accounts for the linear response of phonons to the excitation laser pulse. Some Bragg reflections display a highly nonlinear strain dependence. The origin of linear and two distinct nonlinear response phenomena is discussed in a conceptually simpler model using the interference of envelope functions that describe the diffraction efficiency of the average constituent nanolayers. The combination of both models facilitates rapid and accurate simulations of UXRD experiments.

⁶ Author to whom any correspondence should be addressed.

A large variety of x-ray optics that can be used to monochromatize, focus and analyze the phase of hard x-rays have been invented and realized. Many of them have become standard tools in x-ray science [1] and some more recent developments include e.g. hard-x-ray interferometers with microelectronvolt resolution [2] and nanointerferometers based on refractive lenses [3]. Of particular interest is understanding the manifold physical processes in solids on atomic length and time scales for which hard x-rays providing a subpicosecond time resolution are mandatory [4–8]. Several methods to modify the time structure of x-ray pulses or pulse trains have been reported [9–11]. The concept of exploiting phonons in solid samples generated by femtosecond laser pulses as an ultrafast gateable x-ray mirror [12] has very recently been experimentally implemented using a layered nanostructure composed of the perovskite oxides SrTiO_3 (STO) and SrRuO_3 (SRO) [13]. The authors observed a giant response of a particular Bragg peak showing an intensity increase by a factor of 25 with a gating time of less than 1 ps. The general mechanism was explained as resulting from the expansion of the metallic SRO nanolayers and the concomitant compression of the STO nanolayers that consequently alters the structure factor of the observed Bragg reflection. The artificial spatial layering period was found to set the time scale of the transient gate and the measured diffraction curves could be simulated rather precisely, however, a detailed understanding of the ultrafast x-ray response required for purpose-oriented designing of nanostructures was lacking.

In this paper, we present a detailed analysis of the simulation of transient Θ – 2Θ x-ray diffractograms of periodically layered epitaxial nanostructures, also called superlattices (SL). We show numerical calculations obtained from combined results of (i) a linear-chain model computing the photoexcited lattice dynamics of a given sample [14] and (ii) fully dynamical x-ray diffraction (XRD) calculations. In the following, we refer to these combined linear-chain and dynamical XRD calculations as LCDX. The predicted features of the transient intensities of SL Bragg reflections—including linear and highly nonlinear responses to phonon amplitudes—are interpreted by a conceptually simpler envelope model (EM) that merely considers homogeneous deformations of the single layers. The EM already demonstrates key features that lead to the distinct nonlinear XRD dynamics of such SLs. A comparison to results of ultrafast x-ray diffraction (UXRD) experiments on two different SLs shows the very high degree of precision achieved by the LCDX. The presented analysis will be very valuable for the interpretation of UXRD data in general, and specifically for creating novel devices based on such nonlinear phenomena that utilize the tailorable x-ray interference in artificial nanostructures.

We test our numerical calculations by applying them to two different epitaxial SL samples both composed of metallic and dielectric perovskite oxides. In particular, we consider the previously investigated SL $[\text{SRO}_{20}/\text{STO}_{38}]_{11}$ [13] and a SL containing the ferromagnetic metal $\text{La}_{0.7}\text{Sr}_{0.3}\text{MnO}_3$ (LSMO), namely $[\text{LSMO}_{23}/\text{STO}_{35}]_{15}$. The index of each component represents the number of perovskite unit cells per layer, and the overall index gives the number of repeat units of the double layer (DL). This structural characterization of the samples was done by matching Θ – 2Θ diffractograms with simulations utilizing dynamical XRD theory according to the Darwin formalism [15]. Figures 1(a) and 2(a) show the XRD measurements (gray bullets) and the corresponding simulations (red solid line) for SRO/STO and LSMO/STO, respectively, without any laser excitation. In the following, we develop the EM that explains the particular

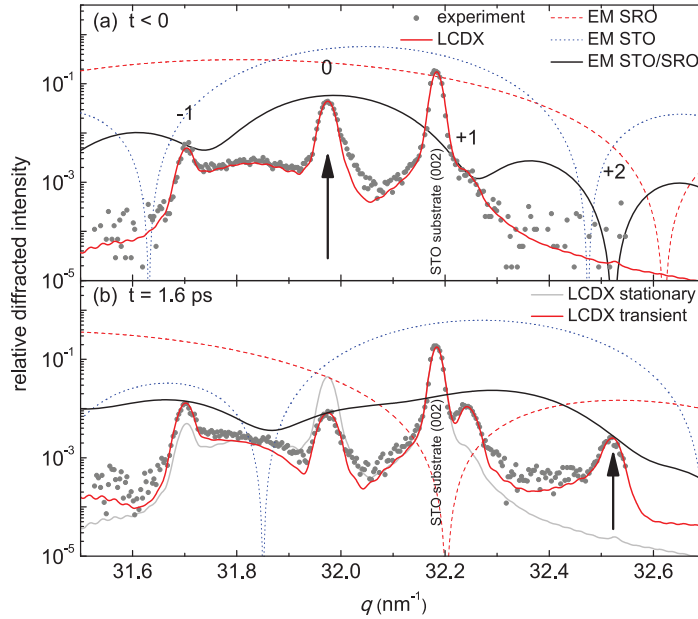


Figure 1. Experimental Θ - 2Θ scans (gray bullets) of the SRO/STO SL. The broken lines show the calculated single-layer envelope functions (scaled for clarity), the black solid line is the DL envelope function (scaled by the number of DL squared), and the red solid line is the resulting SL diffractogram of the LCDX at (a) $t < 0$ and (b) $t = 1.6$ ps after optical excitation with a fluence of 36.8 mJ cm^{-2} . The arrows mark the SL peaks considered in figure 3.

shape of these diffraction curves and provides a fundamental understanding of transient changes upon photoexcitation by femtosecond laser pulses.

As the thickness of the individual layers in both SLs is much smaller than the extinction depth ξ of the x-rays, the corresponding diffractograms are essentially the Fourier transform of their electron densities. Figures 1 and 2 show the square modulus of the diffracted x-ray amplitude $A_M(q)$ ($A_I(q)$) for a single metallic (insulating) layer of the respective sample as a red dashed (blue dotted) line. These curves match a sinc^2 function (the Fourier transform of a homogeneous slab), and we will refer to such curves as envelope functions. The width Δq of such envelope functions is inversely proportional to the real-space thickness d of the respective layer and their center position q_{env} encodes the average strain of that single layer. The envelope of one DL, $|A_{\text{DL}}|^2 = |A_M + A_I|^2$ (black line in figures 1 and 2) accounts for interference of the complex single-layer amplitudes⁷. The DL envelope is scaled by the respective number of DL squared. Clearly, it determines the intensity of the observed SL Bragg reflections since the SL Bragg peaks touch the DL envelope in figures 1(a) and 2(a). In other words, the observed intensity $I(q_{\text{SL}}, t)$ of a particular SL reflection at q_{SL} can be estimated from the relation $I \propto |A_{\text{DL}}|^2$. The SL Bragg peaks thus ‘sample’ the DL envelope at discrete wavevectors that are selected by the Laue condition $q_{\text{SL}} = n \cdot \frac{2\pi}{d_{\text{SL}}} = n \cdot g_{\text{SL}}$, where g_{SL} is the reciprocal lattice vector corresponding to the SL period $d_{\text{SL}} = d_M + d_I$ and $n \in \mathbb{N}$. The single-layer envelope functions themselves have significant intensity only in the q -range around the bulk Laue conditions

⁷ To be precise, one also has to account for the phase shifts due to transmission through the top layer before and after the reflection from the bottom layer. This effect is accounted for in the calculations.

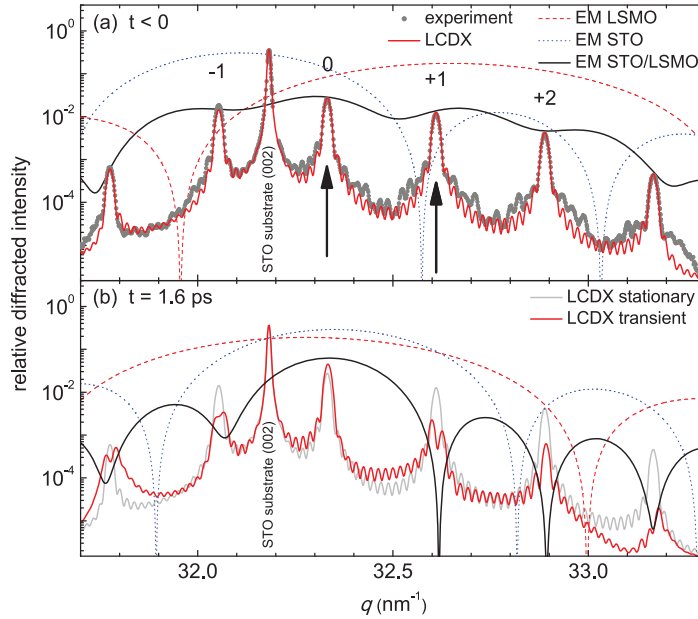


Figure 2. Experimental Θ – 2Θ scans (gray bullets) of the LSMO/STO SL recorded at the EDR-beamline of BESSY II (Helmholtz–Zentrum Berlin). The meaning of the lines and panels is analogous to figure 1, and the arrows mark the SL peaks considered in figure 4.

$q_{M/I} = m \cdot \frac{2\pi}{c_{M/I}}$, where $c_{M/I}$ are the out-of-plane lattice constants of the metal and the insulator, respectively, and $m \in \mathbb{N}$.⁸ For materials with similar c_M and c_I , we number the SL reflections as satellites to the Laue condition $q^{(0)} = \frac{2\pi}{c_{av}} = 2\pi(n_M + n_I)/(n_M c_M + n_I c_I)$ of the so-called zero-order SL peak (ZOP) corresponding to the average lattice constant c_{av} in one DL [16]. Here n_M and n_I correspond to the number of unit cells in the metallic and insulating layers, respectively.

We can now use the above introduced EM to predict the general features of transient changes of diffractograms after laser-pulse excitation such as presented in figure 1. The ultrafast deposition of the excitation energy in the metallic layers of the SL triggers their impulsive expansion [13] which shifts the red dashed envelope to smaller q values. The concomitant compression of STO shifts the blue dotted envelope to larger q values (compare the envelopes in panels (a) and (b) of figures 1 and 2). The magnitude of the envelope shifts is determined by the amplitude of this collective, spatially and temporally periodic lattice motion also referred to as SL phonon mode [14, 17]. As a consequence, the DL envelope function and thus the SL Bragg peak intensities are altered. Eventually, the entire SL will expand within the time $T_{exp} = D/v_{SL}$, where D and v_{SL} are the total SL thickness and the sound velocity in the SL, respectively. For small time delays $t \ll T_{exp}$, however, the SL period remains approximately constant and the SL Bragg peak positions q_{SL} do not change [18]. Here, we exclusively focus on these short-time dynamics.

The UXRD experiments were performed at the FEMTO-slicing beamline of the Swiss Light Source (SLS), providing a time resolution of 140 ± 30 fs [19]. The samples were excited

⁸ In this paper, we exclusively consider the bulk (002) reflections.

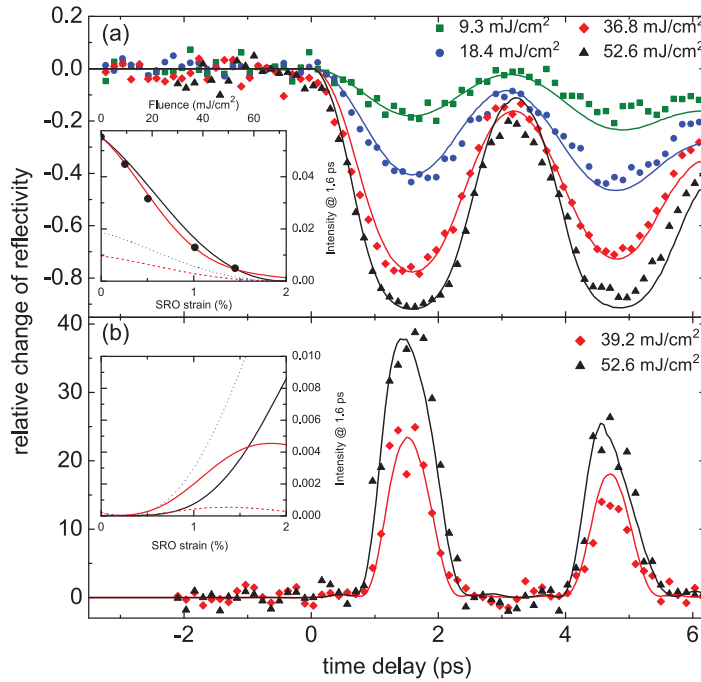


Figure 3. Relative change of Bragg intensity of (a) the ZOP and (b) the +2 SL peak for the SRO/STO SL after optical excitation with different pump fluences. The solid lines represent LCDX calculations. The insets show the calculated SL peak intensities at 1.6 ps according to the EM (black solid line) and LCDX (red solid line). Also, the contributions from individual layers are shown (broken lines). The inset in panel (a) also includes the corresponding experimental data obtained from the transients (bullets).

by ~ 120 fs pump pulses at 800 nm wavelength where the optical penetration depths $\xi_{\text{SRO}} \approx 52$ nm and $\xi_{\text{LSMO}} \approx 90$ nm generate an exponentially decaying stress pattern along the SL stack that is correctly accounted for in the LCDX [14, 20, 21]. As an example, the gray bullets in figures 1(a) and (b) show the measured Θ - 2Θ scans of the STO/SRO SL before and 1.6 ps after excitation, respectively, encompassing four SL reflections (-1 to $+2$). We also recorded the intensity of selected SL Bragg peaks as a function of time delay for different pump fluences. The symbols in figures 3 and 4 illustrate the strong modulations of the relative intensity change $[I(t) - I_0]/I_0$ where $I(t)$ is the measured x-ray intensity at time delay t and I_0 is the measured unpumped signal. Here, it is directly verified that the maximum expansion of the metallic layers of both the SRO/STO and the LSMO/STO SL is reached after 1.6 ps.

In the following, we discuss the simulation of UXRD data. We highlight the linear and nonlinear response of distinct Bragg reflections of the two SLs, starting with the ZOP of the SRO/STO SL. The DL envelope of the excited SRO/STO SL in figure 1(b) matches the experimental SL peak intensities very well, if we assume a homogeneous SRO expansion of 1.3% for a laser fluence of 36.8 mJ cm^{-2} . Only the +1 SL peak close to the substrate peak is overestimated by the EM⁹. If we use the LCDX, we are able to properly calculate the x-ray

⁹ The overestimation of the +1 peak remains even if the complete SL including the substrate is simulated according to the EM (see [13]). This discrepancy between the EM and the exact LCDX is thus due to the inhomogeneous excitation density along the SL stack.

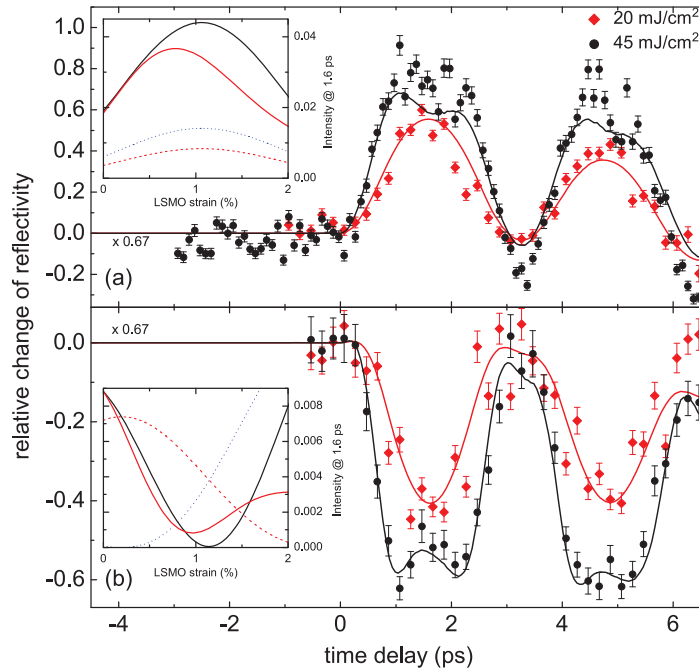


Figure 4. Relative change of the Bragg intensity of (a) the ZOP and (b) the +1 SL peak for the LSMO/STO SL. See figure 3 and the text for plot details.

curve of this particular sample at each point in time and for any strain amplitude. The resulting red line in figure 1(b) shows excellent agreement with the experimental data at 1.6 ps, assuming an average SRO strain of 1.1%.

The photoinduced structure dynamics discussed above lead to a strong decrease of the ZOP intensity with increasing SRO strain, as can be seen in figure 3(a) [13]. According to the EM, this is because the ZOP is governed by the steep flanks of the mutually departing single-layer envelopes. The inset of figure 3(a) compares the ZOP intensity at 1.6 ps as measured (black bullets) and as predicted by the EM (black line) and LCDX (red line). In addition, the contributions of the metallic (red dashed) and insulating (blue dotted) layers are indicated. The EM already yields very good qualitative agreement and illustrates the wide range of linearity up to $\sim 1\%$ average SRO strain. Notably, the LCDX precisely matches the measured ZOP intensity at 1.6 ps (inset). Furthermore, it even accurately reproduces the recorded time scans in figure 3(a). For the highest pump fluence, we deduce an average SRO strain of 1.45% at 1.6 ps.

In the case of SRO/STO ZOP, the linear regime is intrinsically limited because at a certain strain level the ZOP intensity has to vanish, which is indeed the case at about 2% SRO strain. At this point, the first-order minima of both single-layer envelopes approach $q^{(0)}$ (cf inset of figure 3(a)).

In addition to this trivial deviation from linearity, other nonlinear x-ray responses could be identified. As seen in figure 1(a), the +2 SL peak is nearly forbidden in the stationary SL because it is enclosed by the first minima of the SRO and STO layer envelopes [13]. Panel (b) shows that this peak exhibits a strongly enhanced intensity at 1.6 ps due to the structural dynamics. The inset of figure 3(b) indicates the highly nonlinear dependence of this reflection on the SRO

expansion as predicted by the EM (black line). A small strain initially suppresses the peak intensity as it completely shifts the minima of the single-layer envelopes to $q^{(+2)}$. Only above a threshold strain of $\sim 0.5\%$ does this peak attain considerable intensity, mainly due to the increase of the STO envelope function (blue dotted line).

A comparison of the experimental transient intensity of the +2 SL peak with the LCDX calculations presented in figure 3(b) again reveals very good agreement. As the SL phonon amplitude builds up, the intensity first remains unchanged within the signal-to-noise ratio of the experiment up to 800 fs, then rapidly increases to its maximum at about 1.6 ps and subsequently drops back to zero where it again remains for 800 fs. This behavior is repeated for the next periods with lower amplitude according to the energy loss of the SL phonon [14]. This ‘gating’ of x-ray Bragg reflectivity has an FWHM duration of $\lesssim 900$ fs around the maximum at 1.6 ps. Although the EM covers all essential features of the +2 SL peak response (nonlinearity, threshold behavior), the inset of figure 3(b) indicates that the EM predictions quantitatively deviate from the precise LCDX simulations.

As a further test of our models, we present experimental and numerical results for the LSMO/STO SL, including similar linear and nonlinear effects. In addition, however, a transient destructive interference of the diffracted components of the individual layers is identified. The $\Theta-2\Theta$ scan of the SL is shown in figure 2. Again, the ZOP of the LSMO/STO SL is located between the individual envelope functions, however this time with interchanged envelope positions of the metallic and insulating layers. According to the EM, this should lead to an increase of the ZOP intensity due to approaching envelope maxima. This is confirmed by the UXRD measurements reported in figure 4(a), which shows the response of the ZOP. The corresponding inset reveals that the EM predicts a linear increase of the ZOP intensity at 1.6 ps up to $\sim 0.5\%$ LSMO strain (black line); at $\sim 1\%$ it reaches a maximum and then even starts to drop again. This non-monotonic dependence can again be understood by the two approaching envelope functions which maximally overlap at an LSMO strain of $\sim 1\%$ where they provide the highest intensity for the ZOP. For higher strain, the ZOP intensity decreases as the envelope maxima separate again. The experimental data at higher pump fluence in figure 4(a) are indeed indicative of this behavior since we observe a clear plateau around 1.6 ps meaning that the turning point has been reached. Once more, the LCDX satisfactorily simulates the data, although the effects are overestimated and thus have to be scaled down to coincide with the experimental data. The reason for this will be discussed below. The inset in figure 4(a) shows that the EM (black line) qualitatively approximates the LCDX (red line).

In the case of other SL peaks, figure 2(b) reveals that the EM yields a crude underestimation of the peak intensities for a homogeneous LSMO strain of 1.15%. We exemplify the underlying mechanism by investigating the +1 SL peak of the LSMO/STO SL at $q^{(+1)} = q^{(0)} + g_{\text{SL}}$ in more detail. Figure 2(b) as well as the inset of figure 4(b) demonstrate that even though both single-layer envelope functions predict a considerable intensity at 1.15% LSMO strain, the DL envelope vanishes. This is caused by the destructive interference of the x-ray waves diffracted from one LSMO and the adjacent STO layer. The experimental data in figure 4(b) indeed show that for high excitation fluence the signal minimum of the transient around 1.6 ps splits up, verifying the destructive interference and the implied non-monotonic dependence on strain. The LCDX (solid lines in figure 4(b)) predicts the relative intensity decrease to be 50% larger compared to what we measured, most likely because the XRD simulations assume a perfect crystal lattice without any kind of disorder or interdiffusion. The simpler EM even predicts a perfect destructive interference of the x-rays which is much less pronounced in the LCDX

calculations since the true strain pattern is taken into account. Thus, it is not surprising that the LCDX still overestimates the effect of the interference. A similar reason holds for the ZOP.

In conclusion, we have presented predictions of combined model calculations simulating the transient strain field dynamics of photoexcited metal/insulator SLs and the induced transient XRD response. We compare these predictions to various UXRD data taken on SRO/STO and LSMO/STO SLs and find excellent agreement for both linear and nonlinear x-ray response to the induced strain. In particular, we have theoretically predicted and experimentally observed a peculiar destructive interference of x-ray waves in an LSMO/STO SL and a highly nonlinear response in an SRO/STO SL. The observations are interpreted by means of a simpler EM connecting the overall x-ray response to the structural dynamics of the individual layers. The EM correctly covers all transient features and often allows quantitative estimations. For precise simulations, the LCDX has to be evaluated. The presented findings emphasize that UXRD experiments can be accurately interpreted to reveal the transient structural dynamics of epitaxial crystals on subpicosecond time scales. They will open paths for simulation-based design of future ultrafast x-ray devices exploiting such nonlinear or interference phenomena that can be tailored into the nanostructures.

Acknowledgments

The time-resolved experiments were performed on the X05LA beamline at the Swiss Light Source, Paul Scherrer Institut, Villigen PSI, Switzerland. We thank the DFG for supporting the project via BA 2281/3-1 and SFB 762.

References

- [1] Authier A 2003 *Dynamical Theory of X-Ray Diffraction* (Oxford: Oxford University Press)
- [2] Shvyd'ko Yu V, Lerche M, Wille H C, Gerdau E, Lucht M, Rüter H D, Alp E E and Khachatryan R 2003 x-ray interferometry with microelectronvolt resolution *Phys. Rev. Lett.* **90** 013904
- [3] Snigirev A, Snigireva I, Kohn V, Yunkin V, Kuznetsov S, Grigoriev M B, Roth T, Vaughan G and Detlefs C 2009 x-ray nanointerferometer based on Si refractive bilenses *Phys. Rev. Lett.* **103** 064801
- [4] Bargheer M, Zhavoronkov N, Woerner M and Elsaesser T 2006 Recent progress in ultrafast x-ray diffraction *Chem. Phys. Chem.* **7** 783–92
- [5] Chergui M and Zewail A H 2009 Electron and x-ray methods of ultrafast structural dynamics: advances and applications *Chem. Phys. Chem.* **10** 28–43
- [6] Johnson S L, Vorobeva E, Beaud P, Milne C J and Ingold G 2009 Full reconstruction of a crystal unit cell structure during coherent femtosecond motion *Phys. Rev. Lett.* **103** 205501
- [7] Lindenberg A M *et al* 2005 Atomic-scale visualization of inertial dynamics *Science* **308** 392–5
- [8] Sokolowski-Tinten K *et al* 2003 Femtosecond x-ray measurement of coherent lattice vibrations near the Lindemann stability limit *Nature* **422** 287–9 (arXiv:10.1038/nature01490)
- [9] Grigoriev A, Dal-Hyun Do, Dong Min Kim, Chang-Beom Eom, Evans P G, Adams B and Dufresne E M 2006 Subnanosecond piezoelectric x-ray switch *Appl. Phys. Lett.* **89** 021109
- [10] Navirian H A, Herzog M, Goldshteyn J, Leitenberger W, Vrejoiu I, Khakhulin D, Wulff M, Shayduk R, Gaal P and Bargheer M 2011 Shortening x-ray pulses for pump-probe experiments at synchrotrons *J. Appl. Phys.* **109** 126104
- [11] Tanaka Y, Hara T, Yamazaki H, Kitamura H and Ishikawa T 2002 Optical switching of x-rays using laser-induced lattice expansion *J. Synchrotron Rad.* **9** 96–8

- [12] Bucksbaum P H and Merlin R 1999 The phonon Bragg switch: a proposal to generate sub-picosecond x-ray pulses *Solid State Commun.* **111** 535
- [13] Herzog M, Leitenberger W, Shayduk R, van der Veen R, Milne C J, Johnson S L, Vrejoiu I, Alexe M and Hesse D 2010 Ultrafast manipulation of hard x-rays by efficient Bragg switches *Appl. Phys. Lett.* **96** 161906
- [14] Herzog M, Schick D, Gaal P, Shayduk R, von Korff Schmising C and Bargheer M 2011 Analysis of ultrafast x-ray diffraction data in a linear-chain model of the lattice dynamics *Appl. Phys. A* [at press](#)
- [15] Als-Nielsen J and McMorrow D 2001 *Elements of Modern X-Ray Physics* (New York: Wiley)
- [16] Bauer G 1996 *Optical Characterization of Epitaxial Semiconductor Layers* (Berlin: Springer)
- [17] Bargheer M, Zhavoronkov N, Gritsai Y, Woo J C, Kim D S, Woerner M and Elsaesser T 2004 Coherent atomic motions in a nanostructure studied by femtosecond x-ray diffraction *Science* **306** 1771–3
- [18] von Korff Schmising C, Bargheer M, Kiel M, Zhavoronkov N, Woerner M, Elsaesser T, Vrejoiu I, Hesse D and Alexe M 2007 Coupled ultrafast lattice and polarization dynamics in ferroelectric nanolayers *Phys. Rev. Lett.* **98** 257601
- [19] Beaud P, Johnson S L, Streun A, Abela R, Abramsohn D, Grolimund D, Krasniqi F S, Schmidt T, Schlott V and Ingold G 2007 Spatiotemporal stability of a femtosecond hard-x-ray undulator source studied by control of coherent optical phonons *Phys. Rev. Lett.* **99** 174801
- [20] Kostic P, Okada Y, Collins N C, Schlesinger Z, Reiner J W, Klein L, Kapitulnik A, Geballe T H and Beasley M R 1998 Non-fermi-liquid behavior of SrRuO_3 : evidence from infrared conductivity *Phys. Rev. Lett.* **2009** 2498–501
- [21] Liu H L, Lu K S, Kuo M X, Uba L, Uba S, Wang L M and Jeng H T 2006 Magneto-optical properties of $\text{La}_{0.7}\text{Sr}_{0.3}\text{MnO}_3$ thin films with perpendicular magnetic anisotropy *J. Appl. Phys.* **99** 043908